APL Bioengineering

RESEARCH ARTICLE | SEPTEMBER 23 2024

A novel stress sensor enables accurate estimation of micro-scale tissue mechanics in quantitative micro-elastography

Kai L. Metzner ; Qi Fang ; Rowan W. Sanderson ; Yen L. Yeow ; Celia Green ; Farah Abdul-Aziz ; Juliana Hamzah ; Alireza Mowla ; Brendan F. Kennedy

Check for updates

APL Bioeng. 8, 036115 (2024)
https://doi.org/10.1063/5.0220309

View Online
Export Citation

Articles You May Be Interested In

A wireless and handheld optical palpation imaging probe for use in breast-conserving surgery

APL Bioeng. (May 2026)

Load-dependent optical coherence tomography attenuation imaging: How tissue mechanics can influence optical scattering

APL Photonics (August 2024)

Multimodal mechano-microscopy reveals mechanical phenotypes of breast cancer spheroids in three dimensions

APL Bioeng. (September 2024)

30 July 2026 11:07:41

AIP Advances
Why Publish With Us?
21DAYS average time to 1st decision
OVER 4 MILLION views in the last year
INCLUSIVE scope
Learn More
AIP Publishing

AIP Publishing

A novel stress sensor enables accurate estimation of micro-scale tissue mechanics in quantitative micro-elastography

Cite as: APL Bioeng. **8**, 036115 (2024); doi: 10.1063/5.0220309
Submitted: 24 May 2024 · Accepted: 10 September 2024 ·
Published Online: 23 September 2024

View Online Export Citation CrossMark

Kai L. Metzner,[1,2,a)] Qi Fang,[1,2] Rowan W. Sanderson,[1,2] Yen L. Yeow,[3] Celia Green,[4] Farah Abdul-Aziz,[5] Juliana Hamzah,[6] Alireza Mowla,[1,2] and Brendan F. Kennedy[1,2,7,8]

AFFILIATIONS

[1]BRITElab, Harry Perkins Institute of Medical Research, QEII Medical Centre, Nedlands, Western Australia 6009, Australia and Centre for Medical Research, The University of Western Australia, Perth, Western Australia 6009, Australia
[2]Department of Electrical, Electronic & Computer Engineering, School of Engineering, The University of Western Australia, Perth, Western Australia 6009, Australia
[3]Systems Biology and Genomics Laboratory, Harry Perkins Institute of Medical Research, QEII Medical Centre, Nedlands, Western Australia 6009, Australia and Centre for Medical Research, The University of Western Australia, Perth, Western Australia 6009, Australia
[4]Anatomical Pathology, PathWest Laboratory Medicine, QEII Medical Centre, Nedlands, Western Australia 6009, Australia
[5]Hollywood Private Hospital, Nedlands, Western Australia 6009, Australia
[6]Targeted Drug Delivery, Imaging & Therapy, Harry Perkins Institute of Medical Research, QEII Medical Centre, Nedlands, Western Australia 6009, Australia
[7]Australian Research Council Centre for Personalised Therapeutics Technologies, Perth, Western Australia 6000, Australia
[8]Institute of Physics, Faculty of Physics, Astronomy and Informatics, Nicolaus Copernicus University in Toruń, Grudziadzka 5, 87-100 Torun, Poland

[a)]**Author to whom correspondence should be addressed:** kai.metzner@research.uwa.edu.au

ABSTRACT

Quantitative micro-elastography (QME) is a compression-based optical coherence elastography technique enabling the estimation of tissue mechanical properties on the micro-scale. QME utilizes a compliant layer as an optical stress sensor, placed between an imaging window and tissue, providing quantitative estimation of elasticity. However, the implementation of the layer is challenging and introduces unpredictable friction conditions at the contact boundaries, deteriorating the accuracy and reliability of elasticity estimation. This has largely limited the use of QME to *ex vivo* studies and is a barrier to clinical translation. In this work, we present a novel implementation by affixing the stress sensing layer to the imaging window and optimizing the layer thickness, enhancing the practical use of QME for *in vivo* applications by eliminating the requirement for manual placement of the layer, and significantly reducing variations in the friction conditions, leading to substantial improvement in the accuracy and repeatability of elasticity estimation. We performed a systematic validation of the integrated layer, demonstrating >30% improvement in sensitivity and the ability to provide mechanical contrast in a mechanically heterogeneous phantom. In addition, we demonstrate the ability to obtain accurate estimation of elasticity (<6% error compared to <14% achieved using existing QME) in homogeneous phantoms with mechanical properties ranging from 40 to 130 kPa. Furthermore, we show the integrated layer to be more robust, exhibiting increased temporal stability, as well as improved conformity to variations in sample surface topography, allowing for accurate estimation of elasticity over acquisition times 3× longer than current methods. Finally, when applied to *ex vivo* human breast tissue, we demonstrate the ability to distinguish between healthy and diseased tissue features, such as stroma and cancer, confirmed by co-registered histology, showcasing the potential for routine use in biomedical applications.

© 2024 Author(s). All article content, except where otherwise noted, is licensed under a Creative Commons Attribution-NonCommercial 4.0 International (CC BY-NC) license (https://creativecommons.org/licenses/by-nc/4.0/). https://doi.org/10.1063/5.0220309

30 July 2026 11:07:41

I. INTRODUCTION

The mechanical properties of tissue are fundamental to tissue functions across a broad scale, from the intracellular level to the organ level.[1–3] In addition, the mechanical properties of tissue are often altered by disease,[4–7] highlighting the significance of measuring tissue mechanics as a biomarker in disease diagnostics. Over the last 25 years, optical coherence tomography (OCT)-based elastography, termed optical coherence elastography (OCE), has been developed, providing the capability to image tissue mechanical properties with micrometer-scale resolution to depths of up to a millimeter below the tissue surface.[8–11] OCE has found application in various fields including ophthalmology,[12] cardiology,[13] dermatology,[14] oncology,[15] and mechanobiology.[16] In OCE, tissue deformation resulting from an applied load is mapped using OCT, and a mechanical model is then used to generate micro-scale images of the tissue's mechanical properties.[11] Compression-based OCE has emerged as one of the most prominent techniques, due to its straightforward loading mechanism, and the ability to perform rapid, three-dimensional (3D) imaging with a relatively high spatial resolution of 5–50 μm over large lateral fields-of-view (FOV) up to several centimeters.[11] In compression OCE, a quasi-static load is applied to the sample surface, and phase-sensitive OCT is typically used to estimate the resulting strain in the sample.[8–11] However, without directly measuring the sample stress, the sample strain provides only a qualitative estimate of elasticity, limiting comparison between different samples or within the same sample over time.

Quantitative compression-based OCE techniques, such as quantitative micro-elastography (QME), have been developed,[17] enabling estimation of elasticity by determining the two-dimensional (2D) axial stress at the sample surface from the deformation of a pre-characterized, compliant stress sensing layer, placed between an imaging window and the sample prior to compression.[17,18] In this approach, pre-characterization of the stress–strain response of the layer enables the determination of stress at the sample surface from experimentally measured layer strain. QME has been demonstrated in several biomedical applications including in oncology, for evaluating tumor margins in breast-conserving surgery,[19,20] and in mechanobiology, where the unique capability to map micro-scale, 3D elasticity over a relatively large lateral FOV of up to several millimeters can contribute to understanding how mechanics affect cell behavior.[16,21,22] The application of QME to tissue engineering[23] has also been proposed, with the potential to more accurately characterize and recreate the micro-mechanical tissue environment.

While initial studies have demonstrated the potential of QME, its routine practical application has been hindered by significant challenges in the current implementation of the stress sensing layer.[24–26] The use of an independent layer introduces arbitrary friction conditions, leading to ambiguous and inaccurate estimation of elasticity.[25–27] To mitigate friction, a lubricant is applied to the contact boundaries; however, the exudation of lubricant necessitates the use of strict protocols and restricts the duration of reliable elasticity estimation.[25] Moreover, it is challenging to control the precise placement of a soft, thin layer on a biological sample, particularly for samples with non-uniform surface topography where the layer may only partially conform to the sample surface, leading to inaccurate elasticity estimation in regions of insufficient contact caused by air bubbles and fluid pockets.[28] As a result, the complexities of lubricating and positioning the layer, which are subjective procedures that are heavily dependent on a broad range of experimental parameters, lead to inaccurate and low repeatability of elasticity estimation,[25] thus largely limiting the use of QME to *ex vivo* studies performed by trained experts.[24] Consequently, a more reliable implementation is essential to facilitate the translation of QME to routine use in biomedical applications.

In this paper, we propose a new method for accurate and reliable elasticity estimation. Instead of minimizing friction, our approach integrates the stress sensing layer with the imaging window, eliminating variations in friction, and thereby significantly improving imaging performance. We validate our novel approach for integrated stress sensing against the existing QME methodology, demonstrating >30% improvement in sensitivity, >8% improvement in accuracy, and improved temporal stability with a permissible acquisition time >3× longer than current methods for a change in elasticity of <5%. In addition, using a tissue-mimicking phantom with a surface roughness replicating that of excised human breast tissue,[28] we demonstrate improved conformity to sample surface topography and the ability to accurately estimate elasticity. Finally, we apply QME with an integrated layer to *ex vivo* human breast tissue, demonstrating the capability to differentiate various tissue features, such as stroma and cancer, validated by co-registered histology.

II. THEORY: INTEGRATED STRESS SENSING IN QME

In QME, the applied stress is estimated from the deformation of a pre-characterized compliant layer. However, the challenging practical use of the layer, requiring its precise placement on the sample surface, and, also, lubrication at the contact interfaces, introduce variations in the boundary conditions. Temporal and spatial changes in friction and non-uniform contact of the layer cause deviations between the layer response in QME and the pre-characterized stress–strain behavior, affecting the accuracy of the estimated stress and resulting elasticity.[25–28]

To address these challenges and achieve a more robust and practical QME implementation, we integrate the stress sensing layer in QME by adhering the layer to the imaging window. This integration eliminates variations in friction and non-uniform contact at the boundary between the imaging window and layer, ensuring a more consistent estimation of stress. However, integrating the layer maximizes friction at the window-layer boundary, which, coupled with the incompressibility of the layer, restricts layer deformation and leads to inaccuracies in the estimated elasticity.[25–27] Importantly, the effect of friction varies with depth and is localized in the region adjacent to the imaging window-layer boundary. Therefore, by using a sufficiently thick layer, it is possible to spatially decouple the region of the layer that is affected by friction, and the portion used for the estimation of the applied stress.

The process of estimating the applied stress in QME is illustrated in Fig. 1 for three different scenarios. First, Fig. 1(a) shows the current QME methodology using an independent layer under the idealized assumption of uniform contact with a flat sample and frictionless boundary conditions. In this case, the axial displacement of the layer is linear with depth, as shown by the green dashed line in Fig. 1(d). Therefore, the layer strain, calculated as the slope of the axial displacement with depth, is constant with depth [green dashed line in Fig. 1(e)]. Thus, accurate estimation of applied stress can be obtained regardless of the layer region used for stress estimation when employing the pre-characterized stress–strain response of the layer. However, it has previously been shown that the difficulty in the practical use of the layer leads to a breakdown in these idealized assumptions, resulting

30 July 2026 11:07:41

© Author(s) 2024

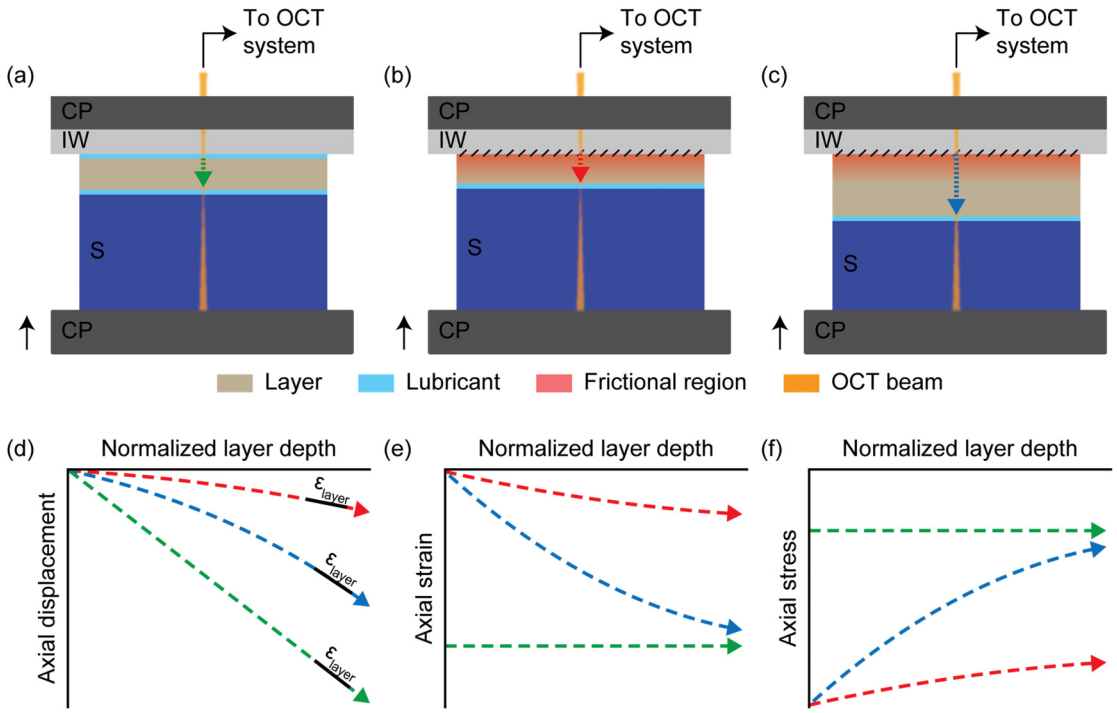

FIG. 1. Estimation of surface stress in QME. (a)–(c) Deformation of the layer under a uniaxial compressive load. (a) Current QME methodology utilizing an independent compliant layer. (b) An integrated layer with the same thickness as the layer illustrated in (a). (c) A thick, integrated layer. The region of the layer affected by friction is indicated by the shaded red region. The plots in (d)–(f) show (d) the layer axial displacement, (e) the layer axial strain, and (f) the estimated applied axial stress as a function of normalized layer depth, enabling comparison between layers of different thickness. Note that the green, red, and blue dashed lines in (d)–(f) correspond to the layer behavior of the current QME methodology, the integrated layer with the same thickness and the thick, integrated layer, as indicated by the vertical, colored arrows in (a)–(c). Additionally, the strain (ε) in the layer is indicated as the slope of solid black lines in (d). CP: compression plate, IW: imaging window, S: sample.

in inconsistent and inaccurate estimation of elasticity.[25–32] A more robust implementation is illustrated in Fig. 1(b), showing an integrated layer of the same thickness as in Fig. 1(a), typically 500–700 μm. In this case, the boundary condition between the imaging window and layer remains fixed, eliminating variabilities arising from changes in friction and non-uniform contact between the imaging window and layer. However, concurrently, friction between the window and layer restricts the axial displacement of the layer, illustrated by the reduced axial displacement in the red dashed line in Fig. 1(d). This results in reduced axial strain in the layer [Fig. 1(e)], and, consequently, an underestimation of the applied axial stress [Fig. 1(f)] compared to the independent layer depicted in Fig. 1(a). This effect is most notable in the region adjacent to the imaging window-layer boundary and diminishes with depth as the impact of friction decreases.[25] Importantly, with a sufficiently thick layer [depicted in Fig. 1(c)], and by estimating the applied stress in the bottom region of the layer, the region affected by friction and the region used for the estimation of surface stress are decoupled. This is shown by the blue dashed lines in Figs. 1(d) and 1(e), where the axial displacement and axial strain in the distal portion of the thick, integrated layer approaches that of the idealized, independent layer illustrated in Fig. 1(a), allowing for accurate estimation of surface stress at the bottom of the integrated layer [Fig. 1(f)].

In addition to variations in boundary conditions between the imaging window and layer, the layer's deformation is influenced by the interface between the layer and sample. At this boundary, through lubrication, and given that the mechanical properties of the layer and sample are typically within the same order of magnitude, the effect of friction can be significantly reduced. However, substantial variations can occur due to spatially varying contact between the layer and sample arising from non-uniform sample surface topography, which has been shown previously to introduce errors in the estimated elasticity.[28] We show that the use of a thick layer, such as that shown in Fig. 1(c), is more robust to variations caused by non-uniform surface topography when compared to an independent layer. The thicker layer ensures better contact between the layer and sample, allowing for accurate estimation of sample elasticity.

III. RESULTS

A. Effect of layer thickness on elasticity accuracy

To investigate the effect of layer thickness on the accuracy of QME with an integrated layer, we performed eight measurements on a homogeneous phantom with Young's modulus (elasticity measured in the linear elastic region) of 49.5 kPa with integrated layers of increasing thickness, ranging from ~0.5 to 3 mm. In each case, the sample elasticity was estimated in a 500 μm (lateral) × 250 μm (axial) region of interest (ROI) in the center of the B-scan, starting from 200 μm below the sample surface.

Figure 2 shows the mean elasticity estimated using integrated layers of varying thickness. The vertical error bars represent the

30 July 2026 11:07:41

© Author(s) 2024

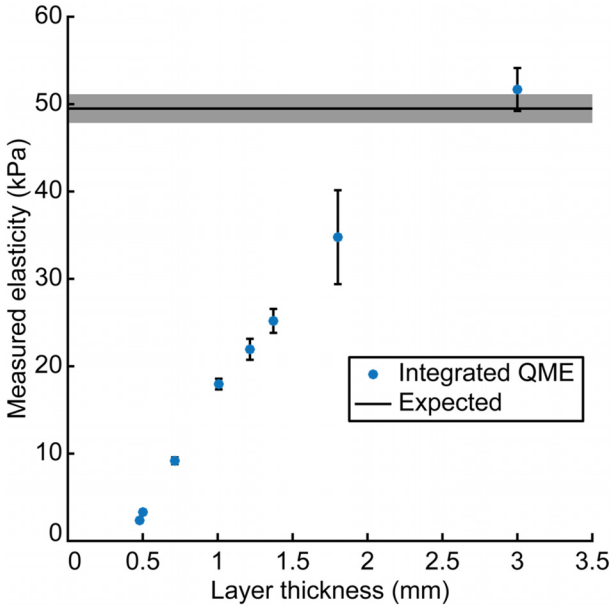

FIG. 2. The mean elasticity estimated using integrated QME with layers of different thicknesses. The vertical error bars show the elasticity sensitivity. The horizontal black line and shaded gray area represent the mean and standard deviation of expected elasticity from uniaxial compression testing.

elasticity sensitivity, defined as the standard deviation of elasticity within the ROI.[25,27] Additionally, the horizontal black line represents the expected sample elasticity, and the shaded gray area shows the standard deviation of the expected elasticity, as measured from nine independent uniaxial compression tests.

In Fig. 2, when performing QME with integrated layers of thickness comparable to those employed in existing QME methodology (typically ∼500–700 μm),[27] a significant underestimation of elasticity is observed. This finding is consistent with previous studies[25,26] showing that, in the absence of lubrication, friction between the imaging window and layer restricts strain in the layer, leading to an underestimation of the applied stress, and, consequently, sample elasticity. For example, the mean elasticity estimated from a layer with a thickness of 0.48 mm was 2.36 kPa, an underestimation by a factor of more than 20. However, as the thickness of the layer is increased, the effect of friction in the region used to estimate the surface stress is reduced, in turn improving the elasticity accuracy. For instance, using a layer with a thickness of 1.8 mm yielded a mean elasticity of 34.8 kPa, an underestimation by a factor of 1.4. For a layer with a thickness of 3 mm, the mean elasticity (51.7 kPa) closely matched the expected elasticity (49.5 kPa), an error of 4.4%, indicating that a thick integrated layer provides accurate estimation of elasticity.

Notably, in Fig. 2, a trade-off is observed between elasticity accuracy and sensitivity for increasing layer thickness. This is apparent from the error bars, which show a reduction in sensitivity from 0.19 to 2.46 kPa as the layer thickness was increased from ∼0.5 to 3 mm. This degradation of elasticity sensitivity is primarily caused by the OCT sensitivity roll-off with depth in the spectral-domain OCT system used, as well as increased strain and translation-induced phase decorrelation noise with depth,[33] described further in Sec. IV.

B. Validation using homogeneous phantoms

In this section, we further validate the performance of QME utilizing an integrated layer with a thickness of 3 mm by performing measurements on four homogeneous phantoms with different elasticities representative of soft tissue, with Young's moduli ranging from ∼40 to 130 kPa.[3,34,35] In each case, the sample elasticity was estimated in a 500 μm (lateral) × 250 μm (axial) ROI in the center of the B-scan, starting from 200 μm below the sample surface. Figure 3 shows the mean elasticity estimated with the independent layer without lubrication (represented by red dots), the independent layer with lubrication (represented by green dots), and the integrated layer (represented by blue dots), with respect to the expected sample elasticity from uniaxial compression testing. The elasticity sensitivity is represented by the vertical error bars, while the horizontal error bars show the standard deviation of the expected elasticity, measured from nine independent uniaxial compression tests. In addition, the solid black line indicates a slope of 1, representing perfect correspondence between the expected and estimated elasticity.

For the independent layer without lubrication (red dots), a significant underestimation of the sample elasticity was observed, with errors ranging from 69% for the softest phantom (elasticity of ∼40 kPa), to 86% for the stiffest phantom (elasticity of ∼135 kPa). By applying a lubricant to the layer, and using an optimized imaging protocol[25] (green dots), the elasticity error is significantly reduced. In this case, an average error of 14% was observed across the four phantoms. In comparison, QME with an integrated layer (blue dots) demonstrated a further improvement in elasticity accuracy, with a mean error

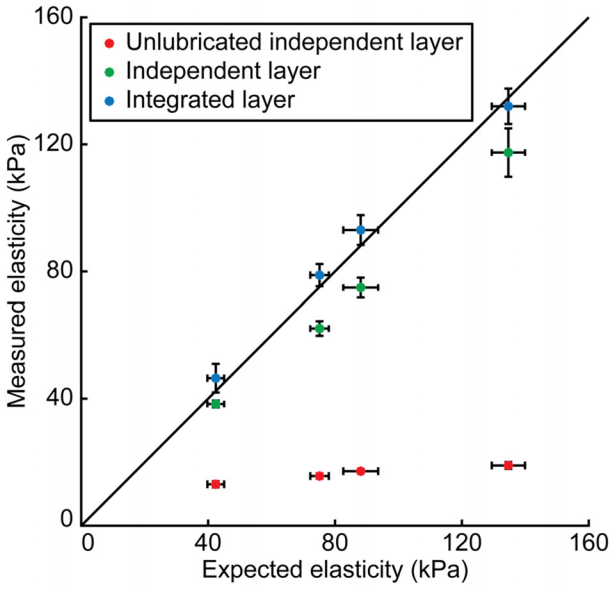

FIG. 3. Validation of the mean elasticity estimated using an independent layer without lubrication (red dots), an independent layer with lubrication (green dots), and an integrated layer (blue dots) on homogeneous phantoms with respect to uniaxial compression testing (expected). The vertical error bars show the elasticity sensitivity and the horizontal error bars indicate the standard deviation of the expected elasticity from uniaxial compression testing. The solid black line represents perfect correspondence between the expected and estimated elasticity.

30 July 2026 11:07:41

© Author(s) 2024

of 6% across the phantoms, demonstrating strong performance over a wide range of sample elasticity.

C. Validation using a heterogeneous phantom

In this section, we demonstrate the capability of QME using an integrated layer with a thickness of 3 mm to provide mechanical contrast in a heterogeneous phantom containing a stiff inclusion. Figure 4 shows OCT B-scans and the corresponding images of sample elasticity (termed micro-elastograms) of the heterogeneous phantom using QME with an independent layer without lubrication [Figs. 4(a) and 4(b)], QME with an independent layer with lubrication [Figs. 4(c) and 4(d)], and QME using an integrated layer [Figs. 4(e) and 4(f)]. For comparison, the mean elasticity and elasticity sensitivity were estimated in a 300 μm (lateral) × 150 μm (axial) ROI in both the bulk and inclusion, indicated by the rectangles in Figs. 4(a)–4(f). Note that when using the integrated layer [Figs. 4(e) and 4(f)], only the bottom ∼500 μm of the layer is imaged to maximize the imaging depth in the sample. To reduce the contribution of edge effects and noise, Figs. 4(a)–4(f) present data in the central 4 mm of the sample, and to a depth of 1.6 mm, where the OCT SNR > 5 dB.

When QME was performed with an independent layer without lubrication [Figs. 4(a) and 4(b)], the mean elasticities of 8.4 and 19.6 kPa estimated in the bulk and inclusion corresponded to an underestimation by more than a factor of five compared to the expected elasticity of 47.1 and 109 kPa of the bulk and inclusion material measured from uniaxial compression testing, respectively. In this case, friction leads to a reduction in contrast between the bulk and inclusion, obscuring the visibility of mechanical features in the micro-elastogram in Fig. 4(b). On the other hand, both QME with an independent layer with lubrication [Figs. 4(c) and 4(d)] and QME with an integrated layer [Figs. 4(e) and 4(f)] yielded relatively accurate estimates of elasticity in the bulk and inclusion. Namely, the mean elasticity and elasticity sensitivity in the bulk were estimated as 48.8 and 5.15 kPa using QME with the independent layer, and 53.4 and 3.48 kPa using the integrated layer, corresponding to errors of 4% and 13% compared to the expected elasticity of 47.1 kPa. Similarly, for the inclusion, the mean elasticity and elasticity sensitivity were estimated as 85.0 and 11.6 kPa using QME with the independent layer, and 84.3 and 7.15 kPa using QME with the integrated layer, corresponding to errors of 22% and 23% compared to the expected elasticity of 109 kPa. The overestimation of elasticity in the bulk and underestimation of elasticity in the inclusion are attributed to the expected elasticity from uniaxial compression testing being performed on a homogeneous sample, and, thus, not incorporating the mechanical interaction between the bulk and inclusion. Namely, the deformation of the softer bulk surrounding the inclusion is constrained by the stiffer inclusion, increasing the apparent elasticity, and vice versa,[25,36] highlighting the importance of considering the heterogeneous nature of samples when evaluating their elasticity.

Notably, QME with an integrated layer showed an improvement in elasticity sensitivity by >30%, estimated as 3.48 kPa in the bulk and 7.15 kPa in the inclusion, compared to 5.15 and 11.6 kPa for the independent layer. This is likely a result of decreased susceptibility to the temporal exudation of lubricant when using the integrated layer, an

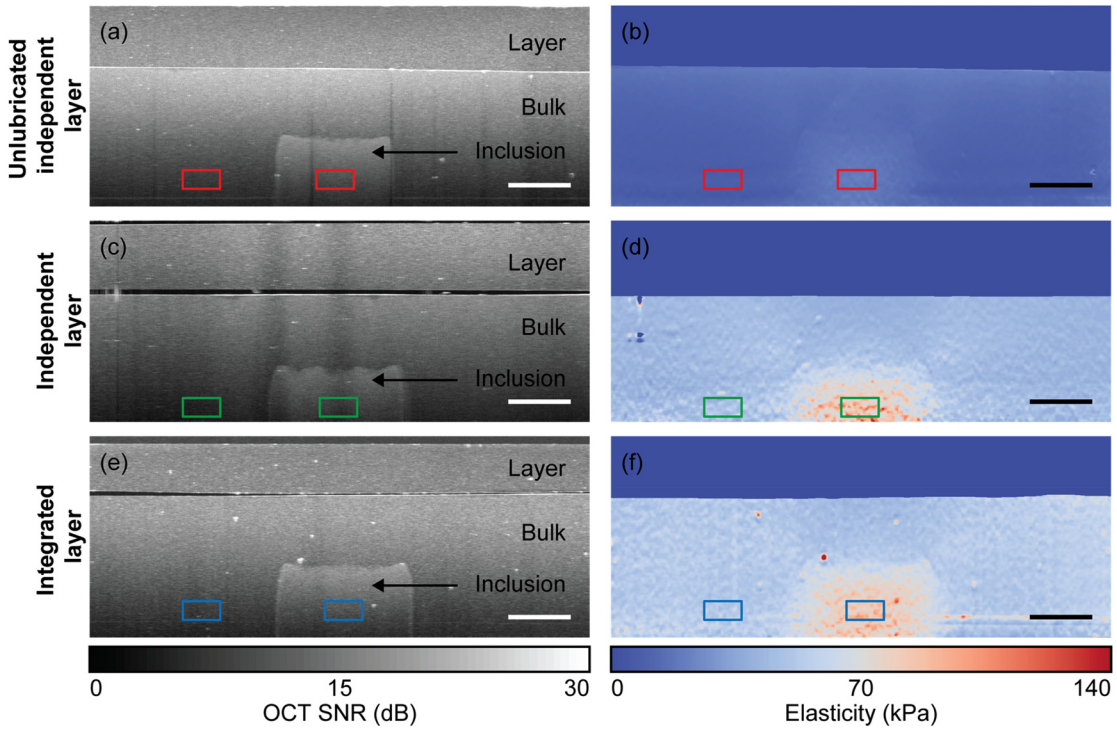

FIG. 4. Estimation of elasticity in a heterogeneous phantom. (a), (c), and (e) show OCT B-scans and (b), (d), and (f) show the corresponding micro-elastograms using an independent layer without lubrication, an independent layer with lubrication, and an integrated layer, respectively. Scale bars represent 500 μm.

30 July 2026 11:07:41

© Author(s) 2024

effect that is known to decrease the elasticity sensitivity.[25,27] This effect is explored in more detail in Sec. III D.

D. Analysis of the temporal stability

In Secs. III B–III C, as well as in previous work, it has been demonstrated that the use of a lubricant has allowed for accurate estimation of elasticity.[25–27] However, it has also been demonstrated that there is a trade-off between elasticity accuracy and the temporal stability of elasticity estimation, caused by the lubricant exuding over time.[25,27] A potential benefit of utilizing an integrated layer with QME is that the requirement for lubrication between the imaging window and layer is removed, improving the accuracy and temporal stability of elasticity estimation. To investigate this, QME scans were performed using an independent layer, and an integrated layer on a homogeneous phantom with Young's modulus of 75.1 kPa. Scans were acquired for 5 min, and the elasticity estimated in a 500 μm (lateral) × 250 μm (axial) ROI in the center of each B-scan, starting from 200 μm below the sample surface. In addition, an identical scan using an independent layer without lubrication was performed to characterize fluctuations in elasticity that occur independent of lubricant exudation. Figure 5(a) shows the mean elasticity estimated from QME with an independent layer without lubrication (red line), an independent layer with lubrication (green line), and an integrated layer (blue line) for 5 min. In each of

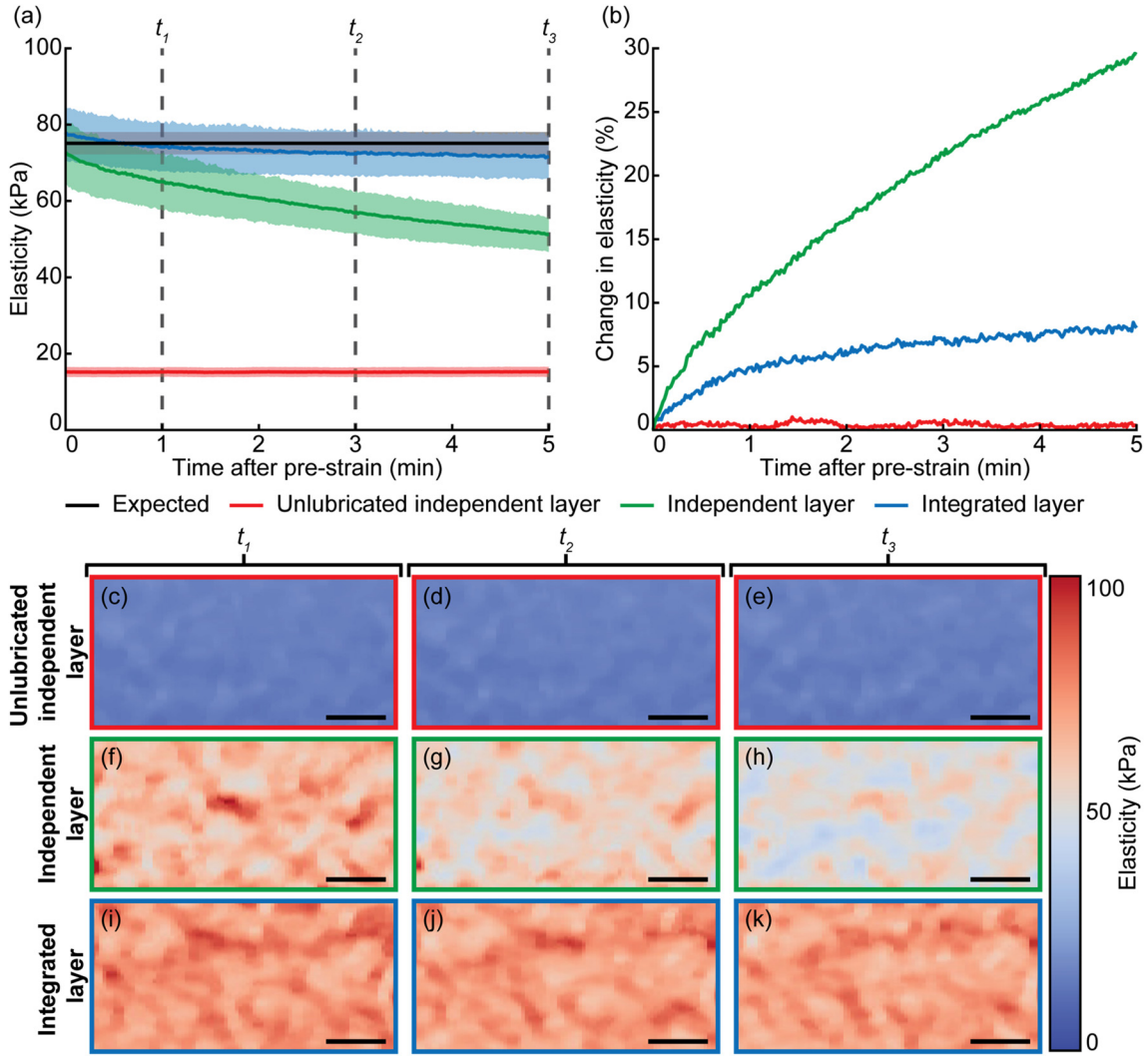

FIG. 5. The estimated elasticity over time using QME. (a) Plots of the mean elasticity (solid line) and elasticity sensitivity (shaded region) estimated using an independent layer without lubrication (red), an independent layer with lubrication (green), and an integrated layer (blue) over 5 min along with the mean and standard deviation of the expected elasticity shown by the solid black line and shaded gray area. (b) Change in the mean elasticity from the initial value for the independent layer without lubrication (red), independent layer with lubrication (green), and integrated layer (blue). (c)–(k) Micro-elastogram ROIs for (c)–(e) the independent layer without lubrication, (f)–(h) the independent layer with lubrication, and (i)–(k) the integrated layer, respectively, where (c), (f), and (i) show the micro-elastograms after 1 min (t_1), (d), (g), and (j) after 3 min (t_2), and (e), (h), and (k) after 5 min (t_3), corresponding to the times shown by the dashed vertical lines in (a). Scale bars represent 100 μm.

30 July 2026 11:07:41

© Author(s) 2024

these cases, the shaded region indicates the elasticity sensitivity within the ROI. The expected elasticity from uniaxial compression testing is indicated by the solid black line and the shaded region indicates the standard deviation of the expected elasticity as measured from nine independent uniaxial compression tests. In addition, to illustrate the temporal stability of each elasticity estimate, Fig. 5(b) shows the percentage change in the mean elasticity compared to its initial value. Furthermore, Figs. 5(c)–5(k) show the micro-elastogram ROIs for QME with an independent layer without lubrication [Figs. 5(c)–5(e)], an independent layer with lubrication [Figs. 5(f)–5(h)] and an integrated layer [Figs. 5(i)–5(k)], after 1, 3, and 5 min, respectively, as indicated in Fig. 5(a) by the dashed vertical lines.

For the control scan without lubrication [red line in Fig. 5(a)], there was minimal temporal change in the mean elasticity over 5 min, where the maximum change from the initial value was $<1\%$ [red line in Fig. 5(b)]. This demonstrates minimal contribution from factors such as system noise and sample viscoelasticity, providing a basis for comparison when assessing QME with the independent and integrated layers, respectively. As expected, despite the high temporal stability of the control scan, there was significant underestimation of the sample elasticity, with a mean error of 80%.

Subsequently, after the application of lubricant to the layer [green line in Fig. 5(a)], there was a clear improvement in the elasticity accuracy, where, for example, the initial mean elasticity was 72.8 kPa, an error of 3.2% with respect to the expected value of 75.1 kPa. However, due to the temporal exudation of the lubricant during acquisition, we observe a change in the mean elasticity of 5% within 20 s and 30% after 5 min [green line in Fig. 5(b)]. This change can also be observed in Figs. 5(f)–5(h), which show the micro-elastogram ROIs after 1, 3, and 5 min, respectively. In this case, to obtain accurate estimation of elasticity with errors $<10\%$, acquisition should be within $\sim$30 s.

When performing QME with an integrated layer, the initial mean elasticity of 78.0 kPa is also in good agreement with the expected elasticity, with an error of 3.8%. In addition, the temporal stability of the elasticity is improved significantly, as is evident in the plot showing the relative change in the mean elasticity in Fig. 5(b). For example, when comparing the allowable acquisition time of the independent layer with lubrication and the integrated layer for a change in elasticity of 5%, the integrated layer allowed for acquisition times $3\times$ longer, with scan times over a minute, compared to $\sim$20 s for the independent layer. In addition, the integrated layer shows a change of only 8% over the entire 5-min acquisition. The improved temporal stability of the integrated layer is further evident in Figs. 5(i)–5(k), which shows comparably little change in the micro-elastogram ROIs with time. The improvement in temporal stability has the potential to enable novel QME methodologies for the comprehensive characterization of micro-scale tissue mechanics, such as non-linear elasticity or viscoelasticity, where in previous implementations, changes in elasticity due to the inherent non-linear elastic and viscoelastic properties of the sample could not be distinguished from changes in elasticity due to lubricant exudation. This longer permissible acquisition time for accurate elasticity estimation could also allow for improved QME image quality by permitting additional temporal averaging.[27]

E. Imaging of a phantom with a rough surface

Tissue often exhibits non-uniform surface topography, requiring pre-strain up to $\sim$20% to achieve sufficient contact with the stress sensing layer.[17,24,28,37] Importantly, variations in the boundary conditions between the layer and sample caused by surface topography have been shown to introduce errors in the estimation of elasticity, even in mechanically homogeneous samples.[28] In this section, using a mechanically homogeneous phantom with a surface roughness replicating that of excised human breast tissue,[28] we demonstrate QME with an integrated layer to be more robust to surface roughness. This was achieved by performing QME using both an independent layer and an integrated layer, where in each case, a pre-strain of 10% was applied to the sample prior to acquisition.

Figure 6 shows images of the surface roughness phantom. Figure 6(a) depicts a 3D visualization of the sample generated using 3D Slicer (v.4.1.1) and STAR-CCM+ (v.15, Siemens AG, Germany) to perform binarization and filtering of an OCT volume of excised human breast tissue,[28] with the dashed circle indicating the 6 mm region scanned in this study. Figure 6(b) shows the surface height map of the phantom measured using OCT. Figures 6(c), 6(d), and 6(e) show the OCT B-scan, *en face* OCT, and *en face* micro-elastogram acquired with the independent layer, respectively. Similarly, Figs. 6(f), 6(g), and 6(h) show the OCT B-scan, *en face* OCT, and *en face* micro-elastogram acquired with the integrated layer. For comparison, the *en face* OCT and *en face* micro-elastograms in Figs. 6(d) and 6(e) and Figs. 6(g) and 6(h) were taken at a depth 50 μm below the layer. Additionally, the B-scans in Figs. 6(c) and 6(f) present data to a depth of 1.6 mm, corresponding to a depth where the OCT SNR >5 dB, with the corresponding locations indicated by dashed lines in the *en face* OCT in Figs. 6(d) and 6(g).

In the *en face* OCT image acquired using the independent layer [Fig. 6(d)], contact with the sample was achieved for 87% of the FOV. When comparing Fig. 6(d) to the surface height map of the phantom in Fig. 6(b), regions of non-contact (regions of low OCT SNR) correspond to valleys within the sample, indicating that the layer did not fully conform to the sample surface. This is further evident in the OCT B-scan in Fig. 6(c), where non-contact between the layer and sample can be seen at the locations corresponding to the two local minima in the surface topography. In comparison, in the *en face* OCT image acquired using the integrated layer [Fig. 6(g)], contact with the sample was achieved for 94% of the FOV. Furthermore, improved contact between the layer and sample can be seen when comparing the OCT B-scan of the integrated layer [Fig. 6(f)] to that of the independent layer [Fig. 6(c)] at the same location.

For the layer to conform to variations in the surface topography, it must deform freely. However, friction acting between the imaging window and layer restricts the deformation of the layer, and, consequently, the ability to conform to the sample surface. In the case of the independent layer, the spatial and temporal exudation of lubricant, especially in regions corresponding to peaks in the sample, restrict the conformation of the layer to variations in the sample surface, leading to regions of non-contact. Conversely, for the integrated layer, given that friction acting between the imaging window and layer is inherently compensated by increasing the thickness of the layer, the distal portion of the layer can conform to variations in the sample surface, hence, providing better contact.

We compared the estimated elasticity using the independent layer and integrated layer from the *en face* micro-elastograms shown in Figs. 6(e) and 6(h), respectively. Note that regions of invalid (negative) elasticity in Figs. 6(e) and 6(h), corresponding to regions of non-contact

30 July 2026 11:07:41

© Author(s) 2024

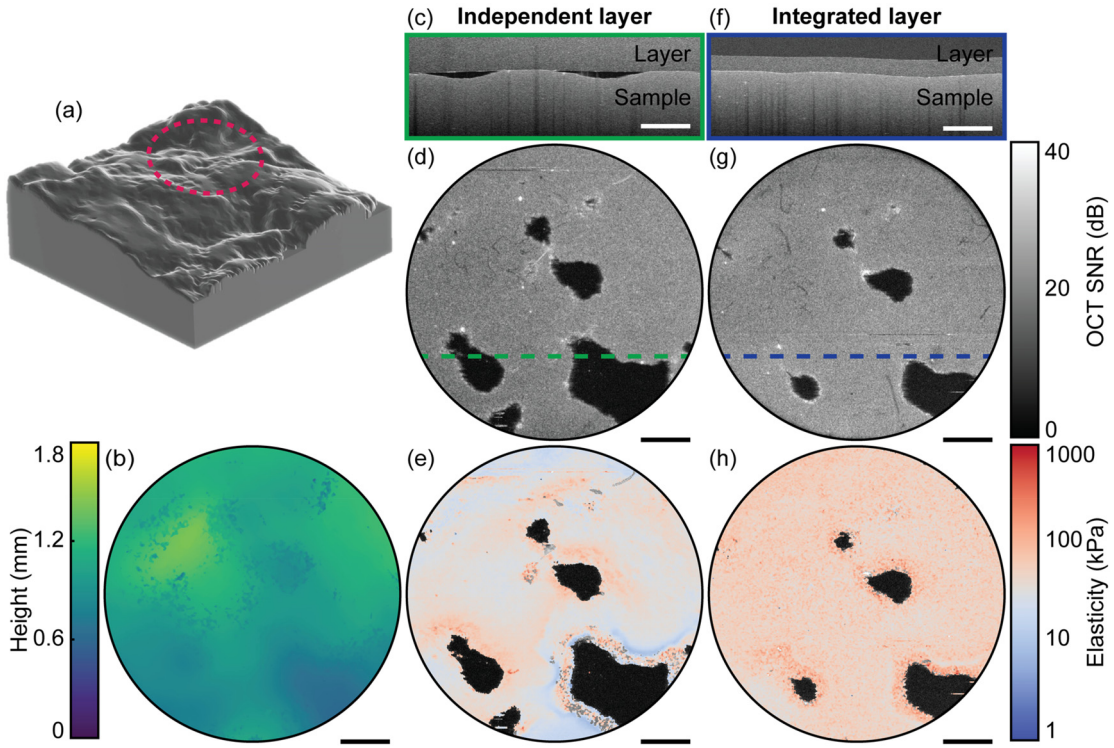

FIG. 6. Tissue phantom that accurately mimics breast tissue surface roughness. (a) and (b) show the 3D model and the surface height map of the phantom, respectively. (c)–(e) Show the OCT B-scan, the *en face* OCT, and the *en face* micro-elastogram using an independent layer, respectively, while (f)–(h) show the OCT B-scan, the *en face* OCT, and the *en face* micro-elastogram using an integrated layer, respectively. Note that the *en face* images in (d) and (e), and (g) and (h) are taken at depths of 50 μm below the layer, and that the locations of the B-scans in (c) and (f) are indicated by green and blue dashed lines in the *en face* OCT in (d) and (g), respectively. Scale bars represent 1 mm.

between the layer and sample, have been masked out and substituted with the corresponding OCT SNR. The mean elasticity and elasticity sensitivity estimated using the independent layer in Fig. 6(e) was 38.6 and 17.4 kPa, respectively, corresponding to an error of 34% compared to the expected elasticity of 58.3 kPa from uniaxial compression testing for the sample material at 10% strain. The underestimation of elasticity in Fig. 6(e) is consistent with previous results, whereby friction resulting from spatial and temporally varying lubrication restricts the deformation of the layer, leading to an underestimation of the applied stress, and, consequently, elasticity.[25,28] In comparison, the accuracy of the estimated elasticity using the integrated layer in Fig. 6(h) is significantly improved, with a mean elasticity of 58.7 kPa and sensitivity of 21.6 kPa, corresponding to an error of $<1\%$.

F. *Ex vivo* imaging of human breast tissue

In this section, we demonstrate QME with an integrated layer on freshly excised human breast tissue removed during a mastectomy procedure. For comparison, we also conducted QME with an independent layer following standard imaging protocols. In both cases, prestrain was applied to the sample prior to imaging to achieve contact and to overcome the non-uniform surface topography.

In postprocessing, image co-registration was performed by matching tissue features in the *en face* OCT images between QME with an integrated layer and QME with the independent layer. For validation purposes, OCT images and micro-elastograms were co-registered with histology of the tissue specimen, stained with hematoxylin and eosin (H&E). In Fig. 7, images of the mastectomy sample are presented, with Figs. 7(a)–7(c) showing the *en face* OCT, strain, and micro-elastogram acquired with the independent layer, respectively, and Figs. 7(d)–7(f) showing scans acquired with the integrated layer. Figure 7(g) shows a histology image of the tissue specimen, with arrows indicating tissue features corresponding to those in Figs. 7(a)–7(f). In addition, to investigate the mechanical contrast between different tissue features, Fig. 7(h) displays a magnified region corresponding to a 0.8×0.8 mm^2 FOV, marked by the blue boxes in Figs. 7(a)–7(g).

The histology image in Fig. 7(g) was annotated by a pathologist and classified as solid papillary carcinoma. Cancerous regions are identified as well-defined solid nodules of neoplastic cells separated by intervening desmoplastic stroma,[38] areas of which are indicated by solid white arrows in Figs. 7(a)–7(g). In addition, regions of interspersed inert stroma are marked by solid black arrows in Figs. 7(a)–7(g). These tissue features are identified in the OCT images in Figs. 7(a) and 7(d). For instance, cancerous areas exhibit moderately low OCT SNR, while stromal regions typically display high OCT SNR.[19,37]

Strain images obtained using both the independent layer and the integrated layer are presented in Figs. 7(b) and 7(e), respectively. In both instances, stromal regions typically exhibit higher magnitudes of negative strain, while cancerous regions display comparatively lower strain. Moreover, several regions of positive strain can be observed

30 July 2026 11:07:41

© Author(s) 2024

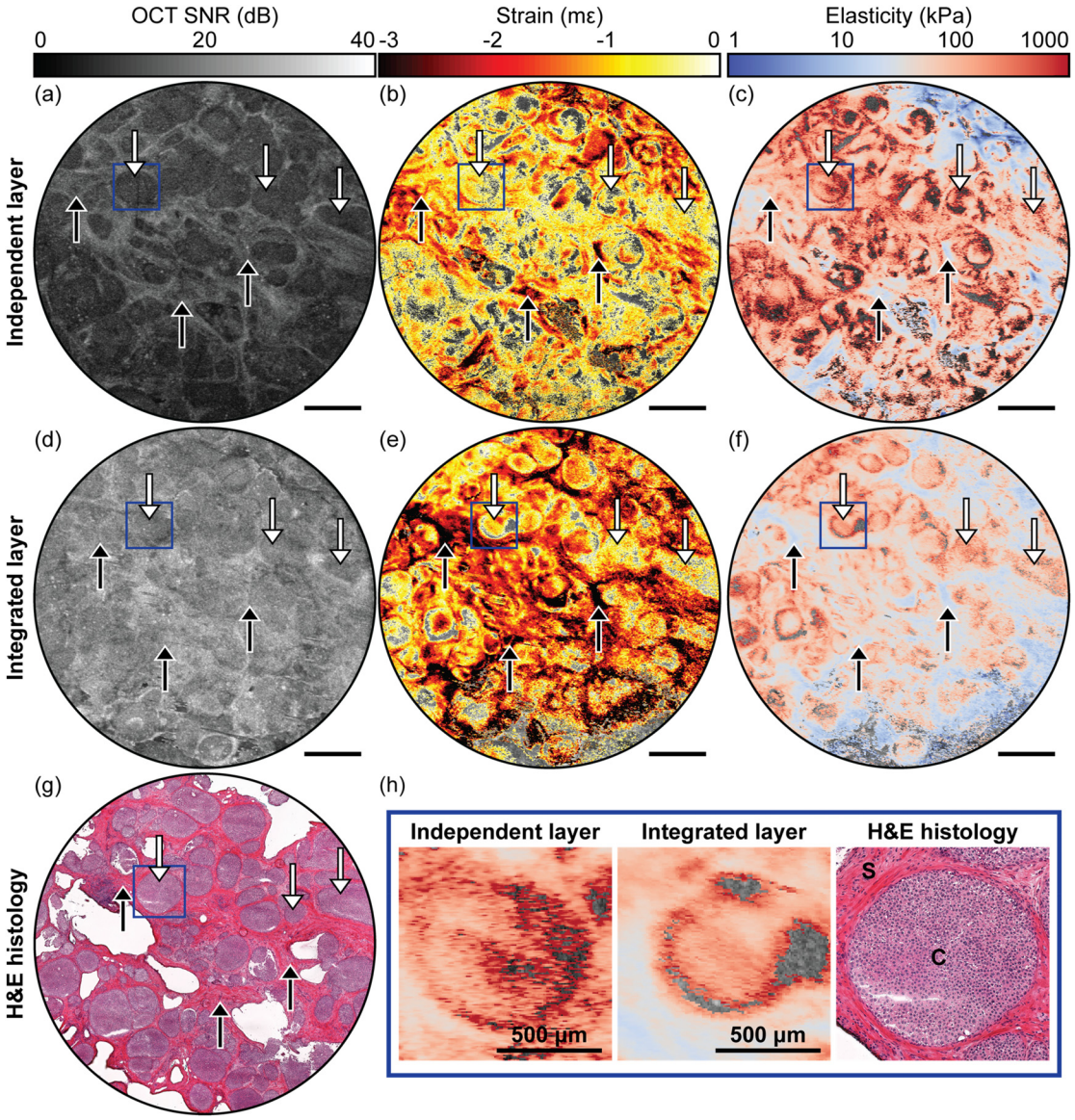

FIG. 7. Imaging of *ex vivo* human breast tissue. *En face* images of (a) OCT, (b) strain, and (c) micro-elastogram using an independent layer. Similarly, (d)–(f) show the corresponding images using an integrated layer at a depth of 50 μm below the sample. (g) H&E histology image of the tissue specimen. Note that the arrows in (a)–(c) for the independent layer, (d)–(f) for the integrated layer, and (g) H&E histology indicate co-registered tissue features, with the solid white arrows indicating regions of cancer and the solid black arrows indicating regions of stroma. (h) Magnified regions of micro-elastograms using the independent layer and integrated layer, alongside H&E histology at the location indicated by the blue boxes in (a)–(g). S: stroma, C: cancer. Scale bars represent 1 mm unless indicated otherwise.

around the periphery of the ducts. This observation aligns with previous studies that have documented positive strain regions at the boundaries of complex tissue features.[17,24,37,39] Given that positive strain regions can lead to invalid (negative) elasticity, they have been masked out in the strain images in Figs. 7(b) and 7(e) and substituted with the corresponding OCT SNR.

Figures 7(c) and 7(f) show micro-elastograms using the independent and integrated layers, respectively. Notably, the mean elasticity estimated across the entire FOV using the independent layer is larger than that of the integrated layer. This increase in mean elasticity estimated with the independent layer is likely due to the higher levels of pre-strain required to achieve contact, resulting in increased elasticity because of the tissue's non-linear elasticity.[40–44] In addition, regions of invalid elasticity in Figs. 7(c) and 7(f) have been masked out and substituted with the corresponding OCT SNR. Consistent with Sec. III E, despite higher levels of pre-strain being applied in the case of the independent layer, the integrated layer shows improved contact, with valid elasticity over 94% of the FOV in Fig. 7(f), compared to 90% for

30 July 2026 11:07:41

© Author(s) 2024

the independent layer in Fig. 7(c). Regardless, in both instances, high mechanical contrast can be observed between different tissue features based on the estimated elasticity. Specifically, cancerous regions, some of which are highlighted by arrows, exhibit increased elasticity compared to surrounding stromal regions, consistent with previous studies.[19,20,45,46] These cancerous regions are particularly distinguishable in the micro-elastogram using the integrated layer [Fig. 7(f)], with improved contrast between regions of cancer and stroma when compared to the independent layer [Fig. 7(c)]. This improvement in contrast is attributed to several factors. First, improved contact between the layer and sample is achieved using the integrated layer, leading to fewer regions of ambiguous elasticity.[28] Additionally, the integrated layer shows improved OCT SNR over the independent layer, with mean OCT SNR of 21.3 and 10.9 dB, respectively. This improvement in OCT SNR is a consequence of the increased temporal stability of the integrated layer, which allows for longer OCT exposure times without compromising accuracy. As a result, higher OCT SNR improves strain sensitivity, and, consequently, elasticity contrast.[27,33,47]

The mechanical contrast between benign and cancerous tissue is further illustrated in the magnified regions in Fig. 7(h), showing a cancerous region surrounded by stroma. The location of this region is indicated by the blue boxes in the micro-elastograms in Figs. 7(c) and 7(f), as well as in the histology image in Fig. 7(g). By segmenting the micro-elastograms in Fig. 7(h) into regions corresponding to stroma and cancer, we obtain estimates of elasticity for each tissue type. For QME with an independent layer, the mean elasticities in the regions of stroma and cancer were estimated as 389 and 1005 kPa, respectively, while for the integrated layer, the elasticities were estimated as 125 and 225 kPa, respectively. For comparison, the elasticity of stroma typically reported in the literature varies from ∼10 to 250 kPa using mechanical testing methods,[34,48] and from ∼5 to 180 kPa using quantitative compression OCE.[17,40,46,49] Similarly, the elasticity of cancerous tumors has been reported from ∼100 to 1300 kPa using mechanical testing methods,[34,48] as well as from ∼100 to 1000 kPa using compression OCE.[17,40,41,45,46,49] The elasticity of stroma and cancer estimated using both the independent layer and the integrated layer align well with values previously reported in the literature. However, the estimation using the integrated layer exhibits closer correspondence, likely due to its capability to achieve contact at lower pre-strain, minimizing the influence of tissue's non-linear mechanical properties. This ensures that the estimated elasticity more accurately reflects Young's modulus, typically used to characterize tissue mechanical properties.[3]

IV. DISCUSSION

In this work, we developed a novel stress sensor, enabling accurate estimation of micro-scale mechanical properties using QME. By integrating a pre-characterized compliant layer with an imaging window, we overcome several key challenges experienced in QME. Through validation of the integrated layer on phantoms and *ex vivo* human breast tissue, we have demonstrated its capability for robust estimation of micro-scale mechanical properties with enhanced accuracy, temporal stability, and practicality, showcasing its potential for routine use in biomedical applications, particularly for users without specialized expertise in QME.

One of the primary advantages of QME with an integrated layer is the substantially improved temporal stability. In the previous implementation using an independent layer, changes in elasticity as large as 10% occur over the acquisition of 1 min, requiring rapid acquisition to ensure accurate elasticity estimation.[25] While this allowed for the estimation of the micro-scale tissue elasticity, it limits the applicability of QME in evaluating additional mechanical properties, such as tissue non-linear elasticity[40,41,44,50] and viscoelasticity,[51–53] which typically require extended acquisition times of several minutes.[42,51,53] By implementing an integrated layer, changes in the boundary conditions due to friction are significantly reduced, allowing for prolonged acquisition times of over 5 min with a change in elasticity of less than 10%, enabling these additional tissue mechanical properties to be estimated using QME. Furthermore, performing multiparametric estimation of the mechanical properties of tissue using QME has the potential to provide complementary contrast for improved differentiation of tissue microstructure,[40,51] and allows for a more comprehensive understanding of tissue mechanical properties,[51,54] facilitating deeper insights into tissue behavior and disease pathology.

A significant barrier to the translation of QME imaging toward clinical application is the impracticality of applying an independent layer on the tissue surface. This approach requires skilled experts for accurate and reliable elasticity estimation and has largely limited QME to *ex vivo* tissue.[20,24,29,49,55] One recent study sought to overcome this, allowing for *in vivo* imaging by replacing the independent layer with a layer that encased the tip of an OCE imaging probe.[19] While simplifying QME implementation, this approach still necessitates lubrication between the imaging window and layer, making it susceptible to the same temporal variations in friction as encountered with the independent layer. In this study, we show that an integrated layer overcomes these challenges, enabling a straightforward implementation that is more robust to variations in friction. In addition, this approach readily facilitates the development of compact QME probes by combining the integrated layer with small imaging probes already demonstrated for OCE imaging.[31,49,56–59] Consequently, QME with an integrated layer improves the applicability of QME for *in vivo* estimation of tissue mechanical properties, with the potential for use in various fields such as cardiology, pulmonology, gastroenterology, and gynecology.

In this study, we have demonstrated that an integrated layer allows for accurate estimation of elasticity with improved sensitivity. However, the maximum imaging FOV of the integrated layer is constrained to 6 mm by the layer geometry. To allow for imaging over larger FOVs, layers of larger diameter can be utilized; however, this concurrently necessitates an increase in the layer thickness to compensate for the restriction of the lateral expansion due to the larger area in contact with the frictional boundary. An important consideration is that QME imaging is typically performed in a common-path configuration for improved phase stability,[39,60–62] limiting the thickness of the layer to ∼2 mm to avoid exceeding the relatively low imaging depth of 2.5 mm (in tissue) of the spectral-domain OCT system used in this study. Moreover, using thicker layers not only reduces the effective imaging depth of the sample,[27] but also degrades elasticity sensitivity due to the considerable OCT sensitivity roll-off with depth of the spectral-domain OCT system, measured as a drop of 19.5 dB over an imaging depth of 3.5 mm in air.[63] To address this, we utilized OCT in a dual-arm configuration for layers thicker than 2 mm, allowing for modification of the axial imaging depth position. However, this configuration increases the susceptibility to mechanical noise, which can significantly reduce strain sensitivity.[39] To overcome this, common-path imaging with thick layers could be achieved by using alternative OCT imaging systems, where, for example, swept-source OCT systems

30 July 2026 11:07:41

© Author(s) 2024

employing vertical-cavity surface-emitting lasers have been shown with low sensitivity roll-off of <5 dB over imaging depths of up to several centimeters,[64–67] offering a viable solution for extending the capabilities of QME with integrated layers.

In this study, we have validated the ability of the integrated layer to provide accurate estimation of elasticity for a range of samples with elasticities representative of biological tissue. While theoretically, samples of arbitrary elasticity can be estimated, the maximum contrast in elasticity between the layer and sample is constrained by the strain dynamic range (the ratio of the maximum to minimum measurable strain) of the QME system. The minimum measurable strain, known as the strain sensitivity, has previously been characterized using a similar imaging system as ∼60 $\mu\varepsilon$,[27] while the maximum measurable strain is limited by the decorrelation of the OCT speckle pattern, which has been reported to occur for strain exceeding ∼5 mε,[33] giving a strain dynamic range of ∼83. For the specific layer used in this study, these parameters allow for the estimation of samples with elasticities ranging from ∼0.6 to 3890 kPa, corresponding to an elasticity dynamic range of 6889 for a given layer. This dynamic range reflects the capabilities of our QME system to estimate a wide range of sample elasticities, while still adhering to the constraints set by the measurable strain limits. To illustrate the ability to achieve accurate estimation of sample elasticity within these constraints, we performed simulations using finite element analysis software (Abaqus 2020, Dassault Systèmes, France), estimating the sample elasticity with a range of layers of different elasticity within the requirements set by the strain dynamic range. Further details on the simulation setup and analysis are included in the supplementary material, including a figure illustrating the layer and sample strain, and sample elasticity for layers of different elasticity.

V. CONCLUSION

In this study, we introduced the development and validation of a novel stress sensor, achieved by integrating a compliant layer directly within a QME imaging system. This integration enables robust and accurate estimation of micro-scale tissue elasticity. We validated the performance of the integrated layer by performing QME on a range of homogeneous phantoms, a heterogeneous phantom, and a phantom replicating the surface topology of *ex vivo* human breast tissue. Our results demonstrate that the integrated layer enables accurate elasticity estimation in homogeneous phantoms, while also offering mechanical contrast with improved sensitivity. Furthermore, we demonstrate that the integrated layer exhibits improved temporal stability, allowing for longer acquisition times, and improved conformity to samples with non-uniform surface topography. Finally, we demonstrated QME with an integrated layer on *ex vivo* human breast tissue, showcasing its ability to provide improved mechanical contrast between cancerous and stromal regions within a tissue specimen. We anticipate that by developing a more robust and practical implementation using an integrated layer, we have laid the groundwork for further translation of QME for the estimation of tissue elasticity in biomedical applications.

VI. METHODS

A. QME system and procedure

A schematic diagram of the QME experimental setup is illustrated in Fig. 8(a). The setup includes a spectral-domain OCT system (TEL320, Thorlabs Inc., USA) comprising a superluminescent diode light source with a central wavelength of 1300 nm and a spectral bandwidth of 170 nm, providing an imaging depth of 3.5 mm and a measured axial resolution of 4.8 μm [full width at half maximum (FWHM)] in air. The scan lens (LSM04, Thorlabs Inc., USA) has a measured lateral resolution of 13 μm and a maximum field of view (FOV) of $16 \times 16\,\text{mm}^2$.[24,28,62] OCT, as an interferometric technique, requires a reference reflection for image formation, typically achieved using either a dual-arm or common-path configuration. Dual-arm OCT provides a reference reflection from a mirror, providing independent control of the reference power, reference position, and OCT focal position. Conversely, the common-path configuration uses a specular reflection within the sample arm as the reference, shown previously to improve phase stability in OCE;[39,60–62] however, this approach restricts the adjustment of the focus position. As such, in this study, common-path was employed for layers thinner than 2 mm due to improved phase stability, while for thicker layers, a dual-arm configuration was used for deeper imaging capability.

The working principle of QME has been described previously.[17] Here, we provide a summary, with the main steps shown in Figs. 8(b)–8(e). QME uses a rigid plate, connected to a motorized stage to apply a pre-strain to the layer and sample situated between the plate and an imaging window. Thereafter, micro-scale strain is applied via an annular piezoelectric actuator attached to an imaging window, and driven by a square wave at a frequency in the quasi-static regime.[68] Actuation is synchronized with OCT imaging to ensure that, at each y-location, a pair of B-scans is acquired in the loaded and unloaded state of micro-scale compression [Fig. 8(b)]. From this, the vector difference of the complex OCT data at each pixel across the FOV is calculated, and the resulting phase angle determined, allowing for an estimation of axial displacement.[62] The local, micro-scale strain in the layer and sample is determined using 1D weighted least squares (WLS) linear regression of the axial displacement [Fig. 8(c)].[62] To estimate the applied stress, we assess the bulk strain in the layer at every lateral location by comparing the original, known layer thickness with the pre-strained thickness using edge detection of the OCT intensity.[18] Combining this with the local layer strain, an estimation of the local, spatially resolved stress in the layer is determined, using the pre-characterized mechanical behavior of the layer material.[17] Figure 8(d) shows the spatially resolved layer stress based on the layer strain in Fig. 8(c) and the pre-characterized mechanical behavior of the layer material. Finally, the micro-elastogram in Fig. 8(e) showing the sample elasticity is estimated by dividing the mean local stress in the layer at each lateral position by the spatially resolved local strain in the sample.[17]

For the results presented in Secs. III A–III D, OCT B-scans were acquired, comprising 1000 A-scans across a 6 mm FOV in the x-direction. At each y-location, a pair of B-scans was acquired, and the vector difference of the complex OCT data calculated at each pixel. For the results presented in Secs. III A–III C, B-scan pairs were acquired at 50 locations across 300 μm in the y-direction in the center of the sample, and the vector difference spatially averaged across the 50 locations to improve strain sensitivity.[47] For the results presented in Sec. III D, analyzing the temporal stability of elasticity estimation, B-scan pairs were repeatedly acquired at ten locations over 60 μm in the y-direction in the center of the sample. Here, the vector difference was spatially averaged across the ten locations, yielding one vector difference measurement per second. For the results on the surface roughness phantom in Sec. III E, an OCT volume with a FOV of $6 \times 6\,\text{mm}^2$ was acquired,

30 July 2026 11:07:41

© Author(s) 2024

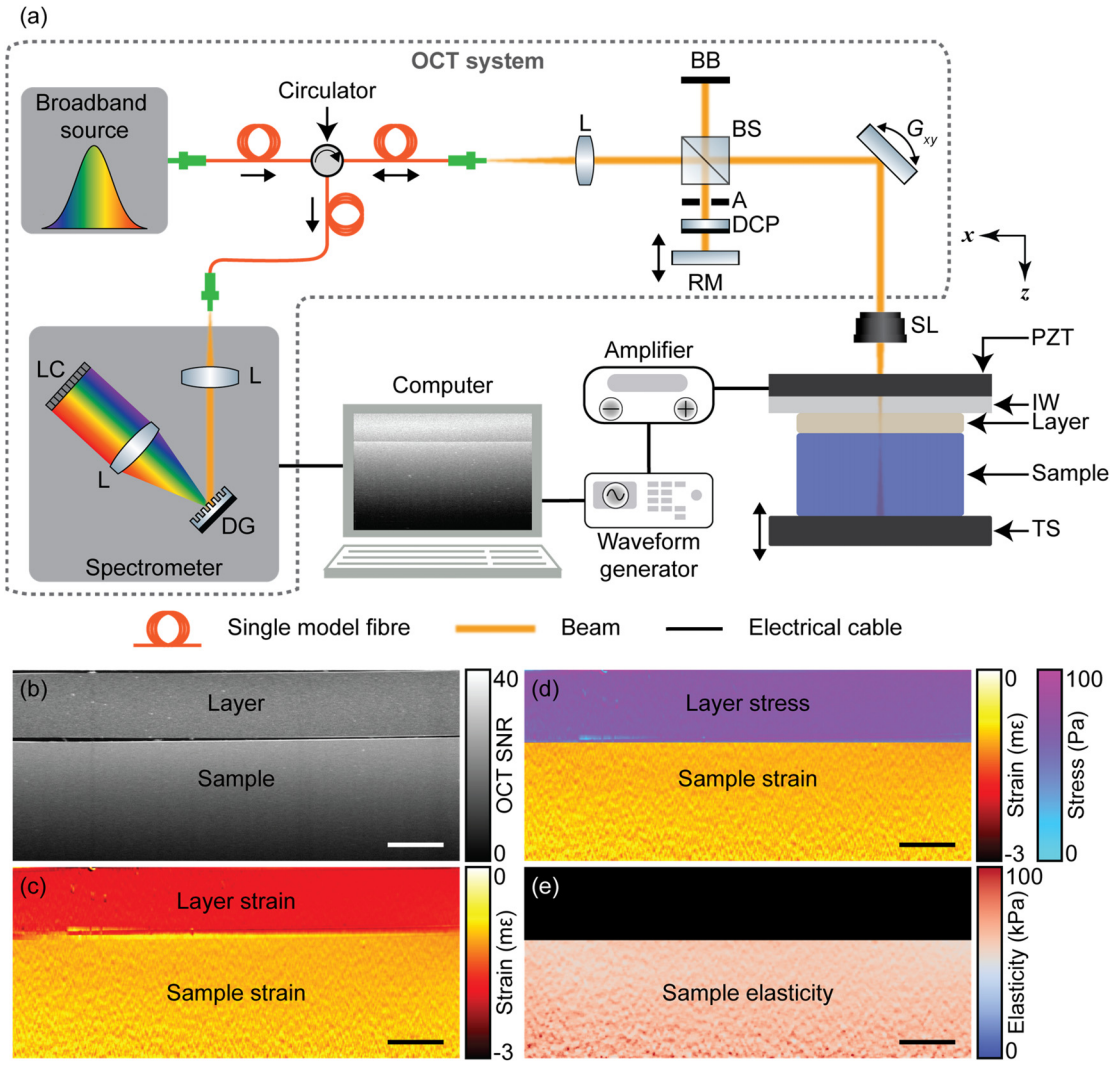

FIG. 8. QME system and procedure. (a) Experimental setup of the QME system, including L: lens, BS: beam splitter, BB: beam block, A: aperture, DCP: dispersion compensation plate, RM: reference mirror, G_{xy}: *xy*-galvanometer, SL: scan lens, DG: diffraction grating, LC: line camera, PZT: lead zirconate titanate ring actuator, IW: imaging window, TS: translation stage. (b)–(e) Working principle of QME. (b) A pair of B-scans acquired in the loaded and unloaded state. (c) Strain in the layer and sample determined using 1D WLS linear regression of axial displacement. (d) Superimposed spatially resolved stress in the layer determined using the layer strain in (c) and the pre-characterized mechanical behavior of the layer material. (e) Micro-elastogram of the sample mechanical properties determined by dividing the local stress in the layer by the local strain in the sample. Scale bars represent 500 μm.

comprising 1000 A-scans per B-scan and 1000 B-scans per volume. Similarly, for the results on *ex vivo* human breast tissue in Sec. III F, scanning with an integrated layer comprised 1000 A-scans per B-scan and 1000 B-scans per volume over a FOV of 6×6 mm^2; however, to aid in image co-registration of the tissue specimen, QME with an independent layer was performed using a larger FOV of 10×10 mm^2, comprising 2000 A-scans per B-scan and 2000 B-scans per volume.

For improved strain sensitivity, in post-processing, the vector difference was convolved with a 2D Gaussian filter, featuring a kernel of 10 μm (lateral) $\times$10 μm (axial) (FWHM). Subsequently, the phase angle is calculated, and the local strain estimated using 1D WLS linear regression with a fitting length of 29 pixels, corresponding to $\sim$100 μm in air.[27,62,69] Using the pre-characterized stress–strain response of the layer, and measurements of the bulk layer strain, and, additionally, the local strain in the layer, the local, axial stress is calculated for each lateral position of the sample. For the results using an integrated layer, for each lateral position, the local strain was axially averaged in the distal 150 μm of the layer, while for QME using an independent layer, the strain was axially averaged in the middle 250 μm of the layer. Finally, the elasticity is determined by dividing the local surface stress by the local strain within the sample. To mitigate high spatial frequency noise in the micro-elastograms, a median filter of 30 μm (lateral) $\times$ 12.5 μm (axial) was applied.

30 July 2026 11:07:41

© Author(s) 2024

For the experiments on phantoms in Secs. III A–III E, lubrication of the contact interfaces was achieved using polydimethylsiloxane (PDMS) silicone fluid (Wacker Chemie AG, Germany) with a kinematic viscosity 100 $mm^2 s^{-1}$, shown previously to yield the highest accuracy over typical QME acquisition times of ∼1 min.[25] For the results on *ex vivo* human breast tissue in Sec. III F, when using an independent layer, lubrication of the window-layer interface was also achieved using a PDMS silicone fluid; however, lubrication of the layer-sample and sample-stage interfaces was achieved consistent with existing clinical protocols developed previously,[17,19] using phosphate-buffered saline.

For the samples presented in Secs. III A–III D, to minimize lubricant exudation, and, therefore, optimize QME accuracy, low pre-strain of <5% was applied to the layer and sample prior to acquisition.[25] In Sec. III E, for the scans of the surface roughness phantom, and Sec. III F for the scans of human breast tissue, to overcome non-uniform surface topography and achieve adequate mechanical loading, larger pre-strains were applied. Namely, for the surface roughness phantom in Sec. III E, a pre-strain of 10% was applied to the sample, while for the scans of human breast tissue in Sec. III F, larger pre-strains of up to 20% were applied to account for the inherent rough surface topography in tissue.

B. Phantom and layer fabrication

The fabrication of layers, four flat homogeneous phantoms, one homogeneous surface roughness phantom, and one heterogeneous phantom was achieved using two-part room-temperature-vulcanizing silicone elastomers (Elastosil P 7676 and Silpuran 2400, Wacker Chemie AG, Germany). The elasticity of the layer and phantoms can be controlled by adjusting the type of elastomer, the mixing ratio, and the addition of a non-cross-linking PDMS silicone fluid (AK50, Wacker Chemie AG, Germany).[70] The mechanical properties of the elastomer materials were characterized using a uniaxial compression device, where in each case, nine independent compression tests of the sample were performed. Characterization yielded Young's modulus of the layer of 46.9 kPa. For the homogeneous phantoms, Young's moduli ranged from 42.4 to 135 kPa. Additionally, the heterogeneous phantom featured a stiff, cubic inclusion with side lengths of ∼1 mm and Young's modulus of 109 kPa, embedded ∼0.6 mm below the surface of a softer bulk with Young's modulus of 47.1 kPa.

The geometry of the layers and phantoms was precisely controlled using 3D printed molds. When fabricating the integrated layers, the silicone elastomer was adhered to the imaging window by directly curing the layer on the imaging window. For the results in Sec. III A, investigating the impact of layer thickness on elasticity accuracy, cylindrical layers were fabricated with a 6 mm diameter and varying thicknesses, ranging from ∼0.5 to 3 mm. For the results in Secs. III B–III F, when using an independent layer in QME, the layers were fabricated with a diameter of 6 mm and thickness of 0.6 mm. Conversely, when performing QME with an integrated layer, a greater thickness of 3 mm was used. The phantoms used in Secs. III A–III D were fabricated with a diameter of 6 mm and a thickness of 3 mm. The fabrication of the surface roughness phantom used in Sec. III E was achieved using a mold replicating the surface roughness of human breast tissue, the development of which has been described previously.[28] A biopsy punch was then used to attain a surface roughness phantom with a diameter of 6 mm, consistent with the other phantoms used in this study.

To provide optical backscattering in the layers and phantoms and improve OCT SNR, titanium dioxide particles (Product No. 232033, Sigma Aldrich, USA) were homogenously mixed into the silicone elastomer prior to curing.[70] For the homogeneous phantoms, and the bulk material of the heterogeneous phantom, titanium dioxide particles were mixed at a concentration of 1 mg/ml. In contrast, the inclusion of the heterogeneous phantom contained a higher concentration of 2.5 mg/ml. Scattering was incorporated into the independent layers at a lower concentration of 0.1 mg/ml. For the thickest layer (3 mm) used in the integrated QME experiments, a bilayer design was adopted to optimize both the OCT SNR in the layer and the imaging depth in the sample. In this design, the top 2.7 mm of the layer is fabricated to be transparent, minimizing optical attenuation, while the bottom 0.3 mm of the layer, which is used for imaging, contains scattering at a concentration of 0.1 mg/ml.

C. Clinical protocol

For this study, an excised mastectomy breast tissue specimen was imaged. Following surgery, the mastectomy sample was dissected by a pathologist in accordance with standard laboratory procedures and hydrated with phosphate-buffered saline solution. The sample was transported on ice from the pathology department to the laboratory where imaging was completed within two hours of excision. Following imaging, the specimen was placed into optimal cutting temperature compound and frozen in liquid nitrogen for sectioning and stained with hematoxylin and eosin for the histological analysis.

SUPPLEMENTARY MATERIAL

See the supplementary material for additional methods detailing the finite element analysis simulation of layer and sample strain, and sample elasticity with layers of different elasticity, and for one supplementary figure.

ACKNOWLEDGMENTS

This study was supported by the Australian Research Council; the Department of Health, Western Australia; the Australian Government Research Training Program Scholarship; and The University of Western Australia University Postgraduate Award. B.F.K. acknowledges funding from the NAWA Chair programme of the Polish National Agency for Academic Exchange and from the National Science Centre, Poland.

AUTHOR DECLARATIONS

Conflict of Interest

B.F.K. reports funding from OncoRes Medical during the conduct of the study and other support from OncoRes Medical: ownership interest (including patents) outside the submitted work; in addition, B.F.K. is an inventor on a patent for a device and a method for evaluating a mechanical property of a material Intl. Pub. No. WO/2016/119011, Appl. No. PCT/AU2016/212695, Priority date: 30/01/2015 issued to OncoRes Medical. No disclosures were reported by the other authors.

30 July 2026 11:07:41

© Author(s) 2024

Ethics Approval

Ethics approval for experiments reported in this paper on human subjects was granted. Written informed consent was obtained and the study approved by the Sir Charles Gairdner and Osborne Park Health Care Group Human Research Ethics Committee (HREC No: RGS01694) and performed in accordance with the relevant guidelines and regulations, including following good clinical practice described at the International Conference on Harmonization.[71]

Author Contributions

Kai L. Metzner: Conceptualization (equal); Data curation (lead); Formal analysis (lead); Investigation (lead); Methodology (equal); Project administration (equal); Writing – original draft (lead); Writing – review & editing (equal). **Qi Fang:** Conceptualization (equal); Formal analysis (supporting); Investigation (equal); Methodology (equal); Supervision (supporting); Writing – review & editing (equal). **Rowan W. Sanderson:** Conceptualization (equal); Data curation (supporting); Formal analysis (supporting); Investigation (equal); Methodology (equal); Writing – review & editing (equal). **Yen L. Yeow:** Data curation (supporting); Investigation (supporting); Resources (supporting); Writing – review & editing (equal). **Celia Green:** Data curation (supporting); Formal analysis (supporting); Investigation (supporting). **Farah Abdul-Aziz:** Investigation (supporting); Resources (supporting); Writing – review & editing (equal). **Juliana Hamzah:** Funding acquisition (supporting); Resources (supporting); Writing – review & editing (equal). **Alireza Mowla:** Conceptualization (equal); Methodology (supporting); Supervision (supporting); Writing – review & editing (equal). **Brendan F. Kennedy:** Conceptualization (equal); Formal analysis (supporting); Funding acquisition (lead); Investigation (equal); Methodology (equal); Project administration (equal); Resources (lead); Supervision (lead); Writing – review & editing (equal).

DATA AVAILABILITY

The data that support the findings of this study are available from the corresponding author upon reasonable request.

REFERENCES

[1]P. Romani, L. Valcarcel-Jimenez, C. Frezza, and S. Dupont, "Crosstalk between mechanotransduction and metabolism," Nat. Rev. Mol. Cell. Biol. **22**(1), 22–38 (2021).

[2]K. H. Vining and D. J. Mooney, "Mechanical forces direct stem cell behaviour in development and regeneration," Nat. Rev. Mol. Cell. Biol. **18**(12), 728–742 (2017).

[3]C. F. Guimarães, L. Gasperini, A. P. Marques, and R. L. Reis, "The stiffness of living tissues and its implications for tissue engineering," Nat. Rev. Mater. **5**(5), 351–370 (2020).

[4]N. M. E. Ayad, S. Kaushik, and V. M. Weaver, "Tissue mechanics, an important regulator of development and disease," Philos. Trans. R. Soc., B **374**(1779), 20180215 (2019).

[5]E. F. Morgan, G. U. Unnikrisnan, and A. I. Hussein, "Bone mechanical properties in healthy and diseased states," Annu. Rev. Biomed. Eng. **20**, 119–143 (2018).

[6]C. T. Mierke, "The fundamental role of mechanical properties in the progression of cancer disease and inflammation," Rep. Prog. Phys. **77**(7), 076602 (2014).

[7]M. C. Lampi and C. A. Reinhart-King, "Targeting extracellular matrix stiffness to attenuate disease: From molecular mechanisms to clinical trials," Sci. Transl. Med. **10**(422), eaao0475 (2018).

[8]B. F. Kennedy, K. M. Kennedy, and D. D. Sampson, "A review of optical coherence elastography: Fundamentals, techniques and prospects," IEEE J. Sel. Top. Quantum Electron. **20**(2), 272–288 (2014).

[9]K. V. Larin and D. D. Sampson, "Optical coherence elastography—OCT at work in tissue biomechanics," Biomed. Opt. Express **8**(2), 1172–1202 (2017).

[10]C. Sun, B. A. Standish, and V. X. D. Yang, "Optical coherence elastography: Current status and future applications," J. Biomed. Opt. **16**(4), 043001 (2011).

[11]B. F. Kennedy, P. Wijesinghe, and D. D. Sampson, "The emergence of optical elastography in biomedicine," Nat. Photonics **11**(4), 215–221 (2017).

[12]M. A. Kirby, I. Pelivanov, S. Song, L. Ambrozinski, S. J. Yoon, L. Gao, D. Li, T. T. Shen, R. K. Wang, and M. O'Donnell, "Optical coherence elastography in ophthalmology," J. Biomed. Opt. **22**(12), 121720 (2017).

[13]H.-C. Liu, M. Abbasi, Y. H. Ding, T. Roy, M. Capriotti, Y. Liu, S. Fitzgerald, K. M. Doyle, M. Guddati, M. W. Urban, and W. Brinjikji, "Characterizing blood clots using acoustic radiation force optical coherence elastography and ultrasound shear wave elastography," Phys. Med. Biol. **66**(3), 035013 (2021).

[14]X. Liang and S. A. Boppart, "Biomechanical properties of in vivo human skin from dynamic optical coherence elastography," IEEE Trans. Biomed. Eng. **57**(4), 953–959 (2010).

[15]W. M. Allen, L. Chin, P. Wijesinghe, R. W. Kirk, B. Latham, D. D. Sampson, C. M. Saunders, and B. F. Kennedy, "Wide-field optical coherence micro-elastography for intraoperative assessment of human breast cancer margins," Biomed. Opt. Express **7**(10), 4139–4153 (2016).

[16]M. S. Hepburn, P. Wijesinghe, L. G. Major, J. Li, A. Mowla, C. Astell, H. W. Park, Y. Hwang, Y. S. Choi, and B. F. Kennedy, "Three-dimensional imaging of cell and extracellular matrix elasticity using quantitative micro-elastography," Biomed. Opt. Express **11**(2), 867–884 (2020).

[17]K. M. Kennedy, L. Chin, R. A. McLaughlin, B. Latham, C. M. Saunders, D. D. Sampson, and B. F. Kennedy, "Quantitative micro-elastography: Imaging of tissue elasticity using compression optical coherence elastography," Sci. Rep. **5**(1), 15538 (2015).

[18]K. M. Kennedy, S. Es'haghian, L. Chin, R. A. McLaughlin, D. D. Sampson, and B. F. Kennedy, "Optical palpation: Optical coherence tomography-based tactile imaging using a compliant sensor," Opt. Lett. **39**(10), 3014–3017 (2014).

[19]P. Gong, S. L. Chin, W. M. Allen, H. Ballal, J. D. Anstie, L. Chin, H. M. Ismail, R. Zilkens, D. D. Lakhiani, M. McCarthy, Q. Fang, D. Firth, K. Newman, C. Thomas, J. Li, R. W. Sanderson, K. Y. Foo, C. Yeomans, B. F. Dessauvagie, B. Latham, C. M. Saunders, and B. F. Kennedy, "Quantitative micro-elastography enables *in vivo* detection of residual cancer in the surgical cavity during breast-conserving surgery," Cancer Res. **82**(21), 4093–4104 (2022).

[20]K. M. Kennedy, R. Zilkens, W. M. Allen, K. Y. Foo, Q. Fang, L. Chin, R. W. Sanderson, J. Anstie, P. Wijesinghe, A. Curatolo, H. E. I. Tan, N. Morin, B. Kunjuraman, C. Yeomans, S. L. Chin, H. DeJong, K. Giles, B. F. Dessauvagie, B. Latham, C. M. Saunders, and B. F. Kennedy, "Diagnostic accuracy of quantitative micro-elastography for margin assessment in breast-conserving surgery," Cancer Res. **80**(8), 1773–1783 (2020).

[21]A. Mowla, J. Li, M. S. Hepburn, S. Maher, L. Chin, G. C. Yeoh, Y. S. Choi, and B. F. Kennedy, "Subcellular mechano-microscopy: High resolution three-dimensional elasticity mapping using optical coherence microscopy," Opt. Lett. **47**(13), 3303–3306 (2022).

[22]D. Vahala, S. E. Amos, M. Sacchi, B. G. Soliman, M. S. Hepburn, A. Mowla, J. Li, J. H. Jeong, C. Astell, Y. Hwang, B. F. Kennedy, K. S. Lim, and Y. S. Choi, "3D volumetric mechanosensation of MCF7 breast cancer spheroids in a linear stiffness gradient GelAGE," Adv. Healthcare Mater. **12**(31), 2301506 (2023).

[23]F. Valente, M. S. Hepburn, J. Chen, A. A. Aldana, B. J. Allardyce, S. Shafei, B. J. Doyle, B. F. Kennedy, and R. J. Dilley, "Bioprinting silk fibroin using two-photon lithography enables control over the physico-chemical material properties and cellular response," Bioprinting **25**, e00183 (2022).

[24]W. M. Allen, K. M. Kennedy, Q. Fang, L. Chin, A. Curatolo, L. Watts, R. Zilkens, S. L. Chin, B. F. Dessauvagie, B. Latham, C. M. Saunders, and B. F. Kennedy, "Wide-field quantitative micro-elastography of human breast tissue," Biomed. Opt. Express **9**(3), 1082–1096 (2018).

[25]K. L. Metzner, Q. Fang, R. W. Sanderson, A. Mowla, and B. F. Kennedy, "Analysis of friction in quantitative micro-elastography," Biomed. Opt. Express **14**(10), 5127–5147 (2023).

30 July 2026 11:07:41

© Author(s) 2024

[26]F. Navaeipour, M. S. Hepburn, J. Li, K. L. Metzner, S. E. Amos, D. Vahala, S. Maher, Y. S. Choi, and B. F. Kennedy, "*In situ* stress estimation in quantitative micro-elastography," Biomed. Opt. Express **15**(6), 3609–3626 (2024).
[27]J. Li, M. S. Hepburn, L. Chin, A. Mowla, and B. F. Kennedy, "Analysis of sensitivity in quantitative micro-elastography," Biomed. Opt. Express **12**(3), 1725–1745 (2021).
[28]R. W. Sanderson, H. T. Caddy, H. M. Ismail, K. Y. Foo, L. J. Kelsey, D. D. Lakhiani, P. Gong, C. Yeomans, B. F. Dessauvagie, C. M. Saunders, B. J. Doyle, and B. F. Kennedy, "Analysis of surface roughness in optical coherence elastography using a novel phantom," Opt. Laser Technol. **169**, 110145 (2024).
[29]E. M. Lloyd, M. S. Hepburn, J. Li, A. Mowla, Y. Hwang, Y. S. Choi, M. D. Grounds, and B. F. Kennedy, "Three-dimensional mechanical characterization of murine skeletal muscle using quantitative micro-elastography," Biomed. Opt. Express **13**(11), 5879–5899 (2022).
[30]V. Y. Zaitsev, A. L. Matveyev, L. A. Matveev, E. V. Gubarkova, A. A. Sovetsky, M. A. Sirotkina, G. V. Gelikonov, E. V. Zagaynova, N. D. Gladkova, and A. Vitkin, "Practical obstacles and their mitigation strategies in compressional optical coherence elastography of biological tissues," J. Innovative Opt. Health Sci. **10**(6), 1742006 (2017).
[31]R. W. Sanderson, A. Curatolo, P. Wijesinghe, L. Chin, and B. F. Kennedy, "Finger-mounted quantitative micro-elastography," Biomed. Opt. Express **10**(4), 1760–1773 (2019).
[32]M. S. Hepburn, P. Wijesinghe, L. Chin, and B. F. Kennedy, "Analysis of spatial resolution in phase-sensitive compression optical coherence elastography," Biomed. Opt. Express **10**(3), 1496–1513 (2019).
[33]L. Chin, A. Curatolo, B. F. Kennedy, B. J. Doyle, P. R. T. Munro, R. A. McLaughlin, and D. D. Sampson, "Analysis of image formation in optical coherence elastography using a multiphysics approach," Biomed. Opt. Express **5**(9), 2913–2930 (2014).
[34]T. A. Krouskop, T. M. Wheeler, F. Kallel, B. S. Garra, and T. Hall, "Elastic moduli of breast and prostate tissues under compression," Ultrason. Imaging **20**(4), 260–274 (1998).
[35]A. Samani, J. Zubovits, and D. Plewes, "Elastic moduli of normal and pathological human breast tissues: An inversion-technique-based investigation of 169 samples," Phys. Med. Biol. **52**(6), 1565 (2007).
[36]K. M. Kennedy, C. Ford, B. F. Kennedy, M. B. Bush, and D. D. Sampson, "Analysis of mechanical contrast in optical coherence elastography," J. Biomed. Opt. **18**(12), 121508 (2013).
[37]B. F. Kennedy, R. A. McLaughlin, K. M. Kennedy, L. Chin, P. Wijesinghe, A. Curatolo, A. Tien, M. Ronald, B. Latham, C. M. Saunders, and D. D. Sampson, "Investigation of optical coherence microelastography as a method to visualize cancers in human breast tissue," Cancer Res. **75**(16), 3236–3245 (2015).
[38]J. Saremian and M. Rosa, "Solid papillary carcinoma of the breast: A pathologically and clinically distinct breast tumor," Arch. Pathol. Lab. Med. **136**(10), 1308–1311 (2012).
[39]B. F. Kennedy, R. A. McLaughlin, K. M. Kennedy, L. Chin, A. Curatolo, A. Tien, B. Latham, C. M. Saunders, and D. D. Sampson, "Optical coherence micro-elastography: Mechanical-contrast imaging of tissue microstructure," Biomed. Opt. Express **5**(7), 2113–2124 (2014).
[40]E. V. Gubarkova, A. A. Sovetsky, L. A. Matveev, A. L. Matveyev, D. A. Vorontsov, A. A. Plekhanov, S. S. Kuznetsov, S. V. Gamayunov, A. Y. Vorontsov, M. A. Sirotkina, N. D. Gladkova, and V. Y. Zaitsev, "Nonlinear elasticity assessment with optical coherence elastography for high-selectivity differentiation of breast cancer tissues," Materials **15**(9), 3308 (2022).
[41]E. V. Gubarkova, A. A. Sovetsky, D. A. Vorontsov, P. A. Buday, M. A. Sirotkina, A. A. Plekhanov, S. S. Kuznetsov, A. L. Matveyev, L. A. Matveev, S. V. Gamayunov, A. Y. Vorontsov, V. Y. Zaitsev, and N. D. Gladkova, "Compression optical coherence elastography versus strain ultrasound elastography for breast cancer detection and differentiation: Pilot study," Biomed. Opt. Express **13**(5), 2859–2881 (2022).
[42]A. A. Sovetsky, A. L. Matveyev, L. A. Matveev, E. V. Gubarkova, A. A. Plekhanov, M. A. Sirotkina, N. D. Gladkova, and V. Y. Zaitsev, "Full-optical method of local stress standardization to exclude nonlinearity-related ambiguity of elasticity estimation in compressional optical coherence elastography," Laser Phys. Lett. **17**(6), 065601 (2020).
[43]Y. Qiu, F. R. Zaki, N. Chandra, S. A. Chester, and X. Liu, "Nonlinear characterization of elasticity using quantitative optical coherence elastography," Biomed. Opt. Express **7**(11), 4702–4710 (2016).
[44]E. V. Gubarkova, D. A. Vorontsov, A. A. Sovetsky, E. L. Bederina, M. A. Sirotkina, A. Y. Bogomolova, S. V. Gamayunov, A. Y. Vorontsov, P. V. Krivorotko, V. Y. Zaitsev, and N. D. Gladkova, "Quantification of linear and nonlinear elasticity by compression optical coherence elastography for determining lymph node status in breast cancer," Laser Phys. Lett. **20**(6), 065601 (2023).
[45]E. V. Gubarkova, E. B. Kiseleva, M. A. Sirotkina, D. A. Vorontsov, K. A. Achkasova, S. S. Kuznetsov, K. S. Yashin, A. L. Matveyev, A. A. Sovetsky, L. A. Matveev, A. A. Plekhanov, A. Y. Vorontsov, V. Y. Zaitsev, and N. D. Gladkova, "Diagnostic accuracy of cross-polarization OCT and OCT-elastography for differentiation of breast cancer subtypes: Comparative study," Diagnostics **10**(12), 994 (2020).
[46]E. V. Gubarkova, A. A. Sovetsky, V. Y. Zaitsev, A. L. Matveyev, D. A. Vorontsov, M. A. Sirotkina, L. A. Matveev, A. A. Plekhanov, N. P. Pavlova, S. S. Kuznetsov, A. Y. Vorontsov, E. V. Zagaynova, and N. D. Gladkova, "OCT-elastography-based optical biopsy for breast cancer delineation and express assessment of morphological/molecular subtypes," Biomed. Opt. Express **10**(5), 2244–2263 (2019).
[47]M. S. Hepburn, K. Y. Foo, P. Wijesinghe, P. R. T. Munro, L. Chin, and B. F. Kennedy, "Speckle-dependent accuracy in phase-sensitive optical coherence tomography," Opt. Express **29**(11), 16950–16968 (2021).
[48]N. G. Ramião, P. S. Martins, R. Rynkevic, A. A. Fernandes, M. Barroso, and D. C. Santos, "Biomechanical properties of breast tissue, a state-of-the-art review," Biomech. Model. Mechanobiol. **15**(5), 1307–1323 (2016).
[49]Q. Fang, L. Frewer, R. Zilkens, B. Krajancich, A. Curatolo, L. Chin, K. Y. Foo, D. D. Lakhiani, R. W. Sanderson, P. Wijesinghe, J. D. Anstie, B. F. Dessauvagie, B. Latham, C. M. Saunders, and B. F. Kennedy, "Handheld volumetric manual compression-based quantitative microelastography," J. Biophotonics **13**(6), e201960196 (2020).
[50]A. A. Plekhanov, M. A. Sirotkina, A. A. Sovetsky, E. V. Gubarkova, S. S. Kuznetsov, A. L. Matveyev, L. A. Matveev, E. V. Zagaynova, N. D. Gladkova, and V. Y. Zaitsev, "Histological validation of in vivo assessment of cancer tissue inhomogeneity and automated morphological segmentation enabled by optical coherence elastography," Sci. Rep. **10**(1), 11781 (2020).
[51]P. Wijesinghe, R. A. McLaughlin, D. D. Sampson, and B. F. Kennedy, "Parametric imaging of viscoelasticity using optical coherence elastography," Phys. Med. Biol. **60**(6), 2293–2307 (2015).
[52]Z. Han, M. Singh, S. R. Aglyamov, C.-H. Liu, A. Nair, R. Raghunathan, C. Wu, J. Li, and K. V. Larin, "Quantifying tissue viscoelasticity using optical coherence elastography and the Rayleigh wave model," J. Biomed. Opt. **21**(9), 090504 (2016).
[53]D. Zhang, C. Li, and Z. Huang, "Relaxation time constant based optical coherence elastography," J. Biophotonics **13**(7), e201960233 (2020).
[54]V. Y. Zaitsev, A. L. Matveyev, L. A. Matveev, A. A. Sovetsky, M. S. Hepburn, A. Mowla, and B. F. Kennedy, "Strain and elasticity imaging in compression optical coherence elastography: The two-decade perspective and recent advances," J. Biophotonics **14**(2), e202000257 (2021).
[55]P. Wijesinghe, D. D. Sampson, and B. F. Kennedy, "Computational optical palpation: A finite-element approach to micro-scale tactile imaging using a compliant sensor," J. R. Soc. Interface **14**(128), 20160878 (2017).
[56]K. M. Kennedy, B. F. Kennedy, R. A. McLaughlin, and D. D. Sampson, "Needle optical coherence elastography for tissue boundary detection," Opt. Lett. **37**(12), 2310–2312 (2012).
[57]K. M. Kennedy, R. A. McLaughlin, B. F. Kennedy, A. Tien, B. Latham, C. M. Saunders, and D. D. Sampson, "Needle optical coherence elastography for the measurement of microscale mechanical contrast deep within human breast tissues," J. Biomed. Opt. **18**(12), 121510 (2013).
[58]Q. Fang, B. Krajancich, L. Chin, R. Zilkens, A. Curatolo, L. Frewer, J. D. Anstie, P. Wijesinghe, C. Hall, B. F. Dessauvagie, B. Latham, C. M. Saunders, and B. F. Kennedy, "Handheld probe for quantitative micro-elastography," Biomed. Opt. Express **10**(8), 4034–4049 (2019).
[59]Q. Fang, A. Curatolo, P. Wijesinghe, Y. L. Yeow, J. Hamzah, P. B. Noble, K. Karnowski, D. D. Sampson, R. Ganss, J. K. Kim, W. M. Lee, and B. F. Kennedy, "Ultrahigh-resolution optical coherence elastography through a micro-

30 July 2026 11:07:41

© Author(s) 2024

endoscope: Towards *in vivo* imaging of cellular-scale mechanics," Biomed. Opt. Express **8**(11), 5127–5138 (2017).
[60]G. Lan, M. Singh, K. V. Larin, and M. D. Twa, "Common-path phase-sensitive optical coherence tomography provides enhanced phase stability and detection sensitivity for dynamic elastography," Biomed. Opt. Express **8**(11), 5253–5266 (2017).
[61]Y. Li, S. Moon, J. J. Chen, Z. Zhu, and Z. Chen, "Ultrahigh-sensitive optical coherence elastography," Light: Sci. Appl. **9**, 58 (2020).
[62]J. Li, E. Pijewska, Q. Fang, M. Szkulmowski, and B. F. Kennedy, "Analysis of strain estimation methods in phase-sensitive compression optical coherence elastography," Biomed. Opt. Express **13**(4), 2224–2246 (2022).
[63]K. Y. Foo, L. Chin, R. Zilkens, D. D. Lakhiani, Q. Fang, R. Sanderson, B. F. Dessauvagie, B. Latham, S. McLaren, C. M. Saunders, and B. F. Kennedy, "Three-dimensional mapping of the attenuation coefficient in optical coherence tomography to enhance breast tissue microarchitecture contrast," J. Biophotonics **13**(6), e201960201 (2020).
[64]I. Grulkowski, J. J. Liu, B. Potsaid, V. Jayaraman, C. D. Lu, J. Jiang, A. E. Cable, J. S. Duker, and J. G. Fujimoto, "Retinal, anterior segment and full eye imaging using ultrahigh speed swept source OCT with vertical-cavity surface emitting lasers," Biomed. Opt. Express **3**(11), 2733–2751 (2012).
[65]S. Moon and E. S. Choi, "VCSEL-based swept source for low-cost optical coherence tomography," Biomed. Opt. Express **8**(2), 1110–1121 (2017).
[66]S. Chen, B. Potsaid, Y. Li, J. Lin, Y. Hwang, E. M. Moult, J. Zhang, D. Huang, and J. G. Fujimoto, "High speed, long range, deep penetration swept source OCT for structural and angiographic imaging of the anterior eye," Sci. Rep. **12**(1), 992 (2022).
[67]F. Xia and R. Hua, "The latest updates in swept-source optical coherence tomography angiography," Diagnostics **14**(1), 47 (2024).
[68]K. J. Parker, L. S. Taylor, S. Gracewski, and D. J. Rubens, "A unified view of imaging the elastic properties of tissue," J. Acoust. Soc. Am. **117**(5), 2705–2712 (2005).
[69]B. F. Kennedy, S. H. Koh, R. A. McLaughlin, K. M. Kennedy, P. R. T. Munro, and D. D. Sampson, "Strain estimation in phase-sensitive optical coherence elastography," Biomed. Opt. Express **3**(8), 1865–1879 (2012).
[70]G. Lamouche, B. F. Kennedy, K. M. Kennedy, C.-E. Bisaillon, A. Curatolo, G. Campbell, V. Pazos, and D. D. Sampson, "Review of tissue simulating phantoms with controllable optical, mechanical and structural properties for use in optical coherence tomography," Biomed. Opt. Express **3**(6), 1381–1398 (2012).
[71]J. R. Dixon, "The international conference on harmonization good clinical practice guideline," Qual. Assur. **6**(2), 65–74 (1999).

30 July 2026 11:07:41

© Author(s) 2024